JOURNAL OF GEOPHYSICAL RESEARCH: OCEANS, VOL. 119, 537–547, doi:10.1002/2012JC008731, 2014

Multiyear sea ice thermal regimes and oceanic heat flux derived from an ice mass balance buoy in the Arctic Ocean

Ruibo Lei,[1] Na Li,[1] Petra Heil,[2,3] Bin Cheng,[4] Zhanhai Zhang,[1] and Bo Sun[1]

Received 6 January 2013; revised 26 November 2013; accepted 21 December 2013; published 22 January 2014.

[1] The conductive and oceanic heat fluxes and the mass balance of sea ice were investigated utilizing an ice mass balance buoy (IMB) deployed in the Arctic Ocean. After IMB deployment, the ice thinned from 1.95 m in late August to 1.46 m by mid-October 2008. From then on, ice growth until mid-June 2009 increased the ice thickness to 3.12 m. The ice temperature and consequently the conductive heat flux at the ice surface exhibited persistent high-frequency variations due to diurnal and synoptic-scale atmospheric forcing. These signals propagated downward with damped magnitude and temporal lag. The competition of oceanic and conductive heat flux dominated the low-frequency variations of ice growth. However, high-frequency variations in ice growth were controlled largely by the oceanic heat flux. From mid-November 2008 to mid-June 2009, the average oceanic heat flux along a track from 86.2°N, 115.2°W to 84.6°N, 33.9°W was 7.1 W/m^2. This was in agreement with that derived from an IMB deployed in 2005, about 1.5° to the north of our buoy. We attributed the relatively high oceanic heat flux (10–15 W/m^2) observed during autumn and early winter to summer warming of the surface ocean. Upward mixing of warm deep water, as observed when our buoy drifted over the shallow region of the Lomonosov Ridge (85.4°–85.9°N, 52.2°–66.4°W), demonstrated the impact of bathymetry on the oceanic heat flux under ice cover, and consequently on the basal ice mass balance.

Citation: Lei, R., N. Li, P. Heil, B. Cheng, Z. Zhang, and B. Sun (2014), Multiyear sea-ice thermal regimes and oceanic heat flux derived from an ice mass balance buoy in the Arctic Ocean, *J. Geophys. Res. Oceans*, *119*, 537–547, doi:10.1002/2012JC008731.

1. Introduction

[2] Arctic sea ice area and thickness have declined dramatically in recent years [*Stroeve et al*., 2012; *Laxon et al*., 2013]. In September 2012, Arctic sea ice extent reached its minimum in the satellite record post 1979. To understand the gravity of the observed changes in Arctic sea ice, it is important to characterize the processes that affect the physical properties of the Arctic sea ice, and to measure its current state. In this study, we focus on the seasonal evolution of the thermal budget of Arctic multiyear sea ice. The vertical gradient of the conductive heat through sea ice, together with the absorbed solar heat, controls the interior energy balance. The conductive heat flux itself depends on the atmospheric and oceanic forcing at the upper and lower boundaries, and is influenced by the snow and sea ice thicknesses [*Lei et al*., 2010].

[3] At its base, the sea ice mass balance is a function of the oceanic heat flux, the conductive heat flux through the ice, and the specific heat flux due to warming or cooling of the ice. The oceanic heat flux itself is a function of heat storage within the upper ocean and of turbulent mixing in the boundary layer [*McPhee*, 1992]. Hence, this flux is controlled by the large-scale oceanic circulation [*Wettlaufer*, 1991], the oceanic stratification [*Shaw et al*., 2009], localized thermal storage from absorption of shortwave radiation [*Perovich et al*., 2011], and the friction at the ice-ocean interface [*Wettlaufer*, 1991]. The oceanic heat flux exhibits a strong spatiotemporal variability. Its seasonal change may reach one order of magnitude. For example, the oceanic heat fluxes at the 1997–1998 SHEBA (Surface HEat Budget of the Arctic Ocean) mass balance sites were only a few W/m^2 during winter and early spring, but increased to more than 15 W/m^2 during summer [*Perovich and Elder*, 2002]. Significant spatial variability, in excess of 20 W/m^2 over 10–100 m horizontally, was identified northeast of Fram Strait [*Wettlaufer*, 1991]. Thus, it is difficult to parameterize the oceanic heat flux under the ice cover for use in numerical models. The reduced Arctic sea ice enables an enhanced oceanic heat flux, due to increased absorption of solar radiation in the upper ocean [*Perovich*, 2011] and accelerated ice drift [*Rampal et al*., 2009].

[1]SOA Key Laboratory for Polar Science, Polar Research Institute of China, Pudong, Shanghai, China.
[2]Australian Antarctic Division, Kingston, Hobart, Tasmania, Australia.
[3]Antarctic Climate and Ecosystems Cooperative Research Centre, University of Tasmania, Hobart, Tasmania, Australia.
[4]Finnish Meteorological Institute, Helsinki, Finland.

Corresponding author: R. Lei, SOA Key Laboratory for Polar Science, Polar Research Institute of China, 451 Jinqiao Rd., Pudong, Shanghai 200136, China. (leiruibo@pric.gov.cn)

2169-9275/14/10.1002/2012JC008731

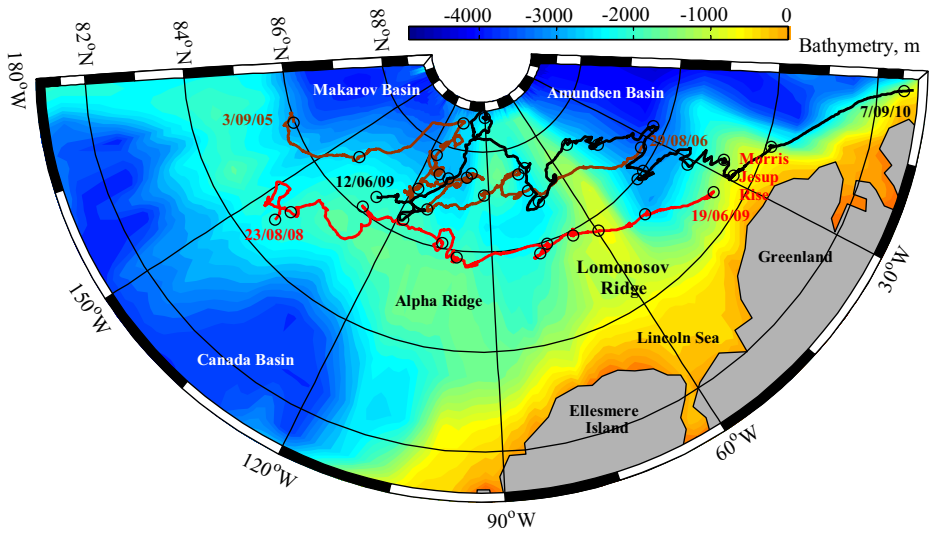

Figure 1. Trajectories of the CHINARE (red), HOTRAX (brown), and ITP29 (black) buoys, with location markers (open circles) every 30 days.

[4] To derive the oceanic heat flux, one may apply oceanic turbulence measurements [*McPhee et al*., 2008; *Timmermans et al*., 2011] or derive it as the residual of the basal ice energy budget, using vertical ice temperature profiles together with the basal ice mass balance [*McPhee and Untersteiner*, 1982]. Since ice temperature profiles and ice mass balance can be acquired by automated buoy or ice-based measurements, the residual-energy method is commonly applied.

[5] Aiming to quantify the thermal regimes of multiyear sea ice in the central Arctic Ocean, we deployed an ice mass balance buoy (IMB) at 84.6°N, 144.1°W over Alpha Ridge in August 2008. Its drift trajectory throughout its 10.5 months lifetime was confined to a narrow zonal swath between 84.0° to 86.5°N (Figure 1), moving across a region where there have been few prior measurements of the ice mass balance. The data are used to study processes contributing to ice mass balance, and to characterize the seasonality of the conductive heat flux within the sea ice and the under-ice oceanic heat flux.

2. Methods and Data

[6] In summer 2008, an IMB was deployed during the third Chinese National Arctic Research Expedition (CHINARE-2008). Technical details for this type of buoy can be found in *Richter-Menge et al.* [2006]. On 19 August 2008, CHINARE-2008 set up an ice camp on a multiyear floe of about 2.5 km^2 at 83.9°N and 144.1°W [*Lei et al*., 2012]. The IMB was deployed on that floe on 22 August 2008. This IMB was composed of three parts: a surface control unit, an acoustic sounder, and a thermistor string. They were set up as an equilateral triangle with 2.5 m side length. Measurement of an electromagnetic induction device showed that the standard deviation of ice thickness along the two orthogonal 50 m profiles centered at the IMB was 0.05 m, implicating level ice. The acoustic sounder was deployed through a 0.10 m diameter borehole, and extended from the borehole about 0.15 m under the ice. The thermistor string of 4.5 m was deployed through a 0.05 m diameter borehole. The spacing of thermistor in the string was 0.10 m. Both accuracy and resolution of the acoustic sensors were 0.01 m, while those of the thermistor string were 0.1 and 0.01 K, respectively. Upon deployment, the snow depth/ice thickness at the sounder and thermistor string sites were 0.05/1.95 and 0.05/1.92 m, respectively. Auxiliary physical properties of the ice were derived from ice cores collected from a nearby site (Figure 2) 2 days after the IMB was installed. The brine and gas volume fractions were calculated as functions of the ice temperature, salinity, and density, according to *Leppäranta and Manninen* [1988]. Most parts of the ice core were above or close to the freezing point. The total porosity (brine plus gas volume fractions) was high, resulting in a low ice density and salinity, especially for the upper 0.8 m of ice.

[7] After deployment, the sea ice with the IMB moved eastward, over the Alpha Ridge into the Makarov Basin, then across the Lomonosov Ridge into the Amundsen Basin (Figure 1). It ceased to transmit data once north of Greenland on 7 July 2009. The thermistor string data showed that the freezing front had reached the ice base by 8 October 2008. We therefore used thermistor data only after that date. All sensors except the upper acoustic sounder worked well throughout the IMB operation. Data from the upper sounder are available from 22 August to 10 October 2008.

[8] The NCEP/NCAR atmospheric reanalysis data of 10 m-height wind speed [*Kistler et al*., 2001] were used to ascertain local atmospheric forcing. Sea ice concentrations were derived from Advanced Microwave Scanning Radiometer-EOS brightness temperatures [*Spreen et al*., 2008]. Averaged ice concentrations over an area 50 km × 50 km were used to characterize the ice conditions around the IMB. Bathymetric data were from the International Bathymetric Chart of the Arctic Ocean [*Jakobsson et al*., 2008]. Data from an IMB deployed by the Healy-Oden Trans-Arctic Expedition (HOTRAX) in September 2005 [*Perovich et al*., 2009] were used to compare its ice mass balance and derived heat fluxes with those from the

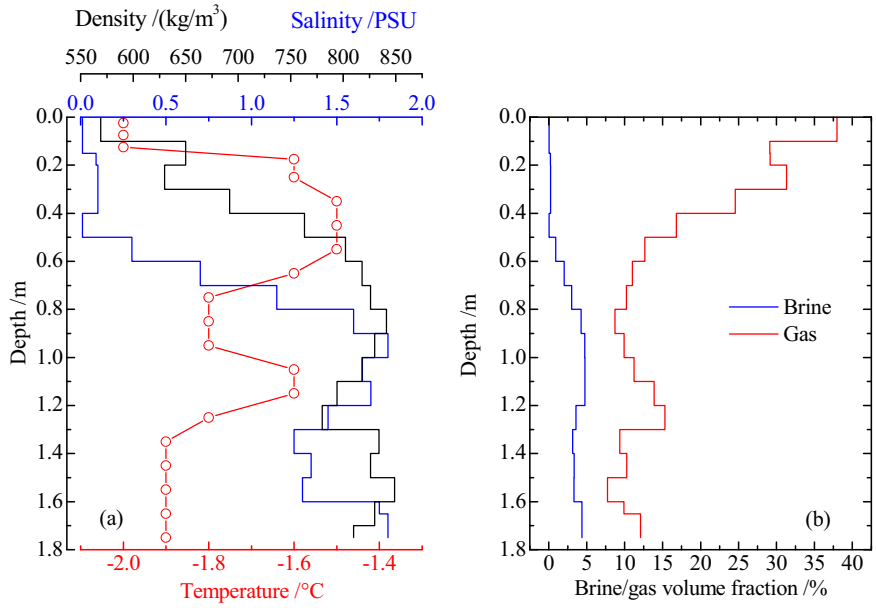

Figure 2. (a) Temperature, salinity, and density and (b) fractions of brine and gas volumes of ice cores collected on 24 August 2008.

CHINARE IMB. Upper-ocean physical data collected by the Ice-Tethered Profiler 29 (ITP29) from 12 June 2009 to 7 September 2010 [*Toole et al*., 2011] were used to assess the oceanic heat flux derived from our IMB. Both the trajectories of the HOTRAX IMB and ITP29 were aligned with, albeit north of the trajectory of the CHINARE IMB.

3. Results

3.1. Environmental Conditions Along IMB Trajectory

[9] At the IMB, the surface air temperature fell below the freezing point in mid-September 2008. From 10 September 2008 to 8 June 2009, the daily average air temperature remained below the freezing point (Figure 3b). The synoptic-scale variations of air temperature during winter exceeded those during summer. For example, during late autumn and winter, air temperature variations in excess of 15 K often occurred within 2 or 3 days. This pattern of short-term variability characterized the surface air temperature, through its absolute minimum in early March 2009. From late March onward, air temperature increased more or less steadily. Finally, it fluctuated around 0°C after mid-June 2009.

[10] Storm activities, accompanied by increased wind speed and warm air advection, occurred about every 6.7 (±3.1) days during much of the IMB's operation (Figure 3c). During storm events wind speed typically exceeded 10 m/s, causing the ice drift to accelerate. Ice drift was relatively fast during autumn, early winter, and summer (averaging 0.10 m/s), and relatively slow in late winter and spring (averaging 0.07 m/s). Ice concentration remained above 90% throughout the entire investigation (Figure 3d). The mean seawater temperature at depths 3.5–4.0 m decreased from −1.55°C in late August 2008, to −1.63°C by the end of April 2009 (Figure 3e). It gradually increased again after the end of June 2009.

3.2. Sea Ice Mass Balance

[11] Snow accumulation at the IMB site was 0.08 m from 22 August to 10 October 2008, due to either new or blowing snow. Melt at the ice base continued until 10 October 2008, yielding a cumulative loss of 0.49 m resulting in an ice thickness of 1.46 m with a mean melt rate of 0.01 m/d over 49 days. The latter corresponded to latent heat flux of 29 W/m^2. Our data demonstrated that the ice base determined by the under-ice sounder and by the thermistor string matched well each other by mid-October 2008. This was evidenced by (1) the freezing front extending to the ice base, (2) the temperature at ice base remaining at the freezing point, and (3) the ice temperature gradient having been established across the basal ice layer (Figure 3f). Although this temperature gradient was very low, it distinctly differentiated this layer from the oceanic mixed layer underneath the ice. The ice growth rate was initially sluggish during October 2008. Post mid-November 2008, the ice growth rates repeatedly exceeded 0.01 m/d (Figure 3g). Thus, the transition from basal decay-freeze balance to distinct growth took about 1 month while heat was released by refreezing of brine pockets and increasing solid fraction within the ice. From 10 October to 12 November 2008, the heat released from ice cover was estimated to be 6.5 MJ/m^2 by using the observed ice temperature by the IMB and the ice salinity and density derived from the ice core measurements. *Perovich et al*. [1997] found a similarly extensive transition for a floe in the Beaufort Sea during both, the deployment year of their IMB and the subsequent year. Thus, we inferred that this process was not related to the disturbance of the borehole by buoy deployment. Our data showed that the ice grew from 1.46 m on 10 October 2008 to an annual maximum of 3.12 m on 11 June 2009, yielding a mean ice growth rate of 0.007m/d. Surface ice melt started earlier than basal ice melt, and was detected after 13

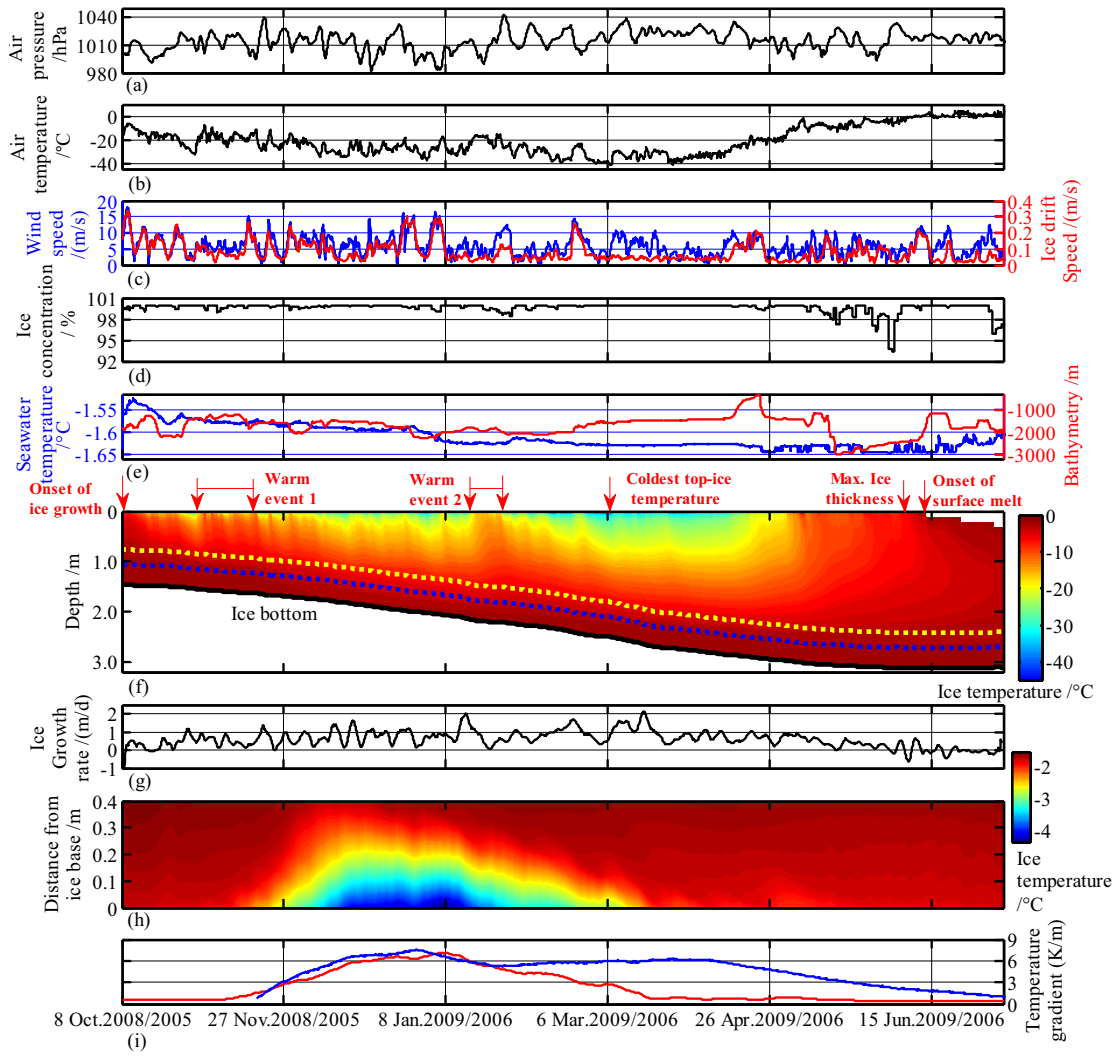

Figure 3. (a) Surface air pressure, (b) air temperature, (c) wind and ice speed, (d) ice concentration, (e) mean seawater temperature at depths 3.5–4.0 m and bathymetry, (f) ice temperature contour, the levels of 0.70 m (yellow dashed line) and 0.40 m (blue dashed line) from ice bottom, and ice bottom (black line), (g) ice growth rate, (h) ice temperature contour within the basal 0.40 m layer, and (i) linear fit ice temperature gradient of this layer (red line) at the CHINARE site. Air pressure and temperature were measured by the IMB, and wind speed was derived from reanalysis data. The corresponding temperature gradient at the HOTRAX site (blue line) also was plotted in Figure 3i.

June 2009, when the temperatures exceeded 0°C near the upper surface.

[12] Lowest sea ice temperatures were generally encountered in the upper layers in response to atmospheric forcing. Extended atmospheric warming events lasted for about 8–15 days in the first half of November 2008 and late January 2009 (Figure 3b). They resulted in marked increases of the ice temperature over the entire ice depth (Figure 3f) and a pronounced decrease of the ice growth rate (Figure 3g). In the deeper layers, the high-frequency variations of ice temperature were damped, and with substantial lag to those at the surface. During the initial ice growth season, as the freezing front approached the ice base, the brine channels refroze from the top of the ice downward, which delayed the ice cooling and resulted in a low ice temperature gradient, especially for the low layer. The linear fit gradient within the basal 0.40 m ice layer increased gradually from mid-November 2008 onward, due to further refreezing of brine pockets (Figures 3h and 3i). The refreezing process of brine pockets within multiyear ice during the initial ice growth season clearly differentiates it from first-year ice [*Lei et al.*, 2010]. For comparison, we also calculated the temperature gradient of the basal 0.40 m ice layer at the HOTRAX site (Figure 3i). This temperature gradient showed a similar seasonality as that at the CHINARE site. Both had relatively small values in November. They distinctly increased in December, and peaked at about 7.1–7.4 K/m in early January. Both series reverted to relatively small values by the end of June due to the seasonal warming of the ice temperature and the decrease in ice growth rate. Both processes might result in a lower solid fraction in the basal ice layer [*Wettlaufer et al.*, 1997; *Hunke et al.*, 2011]. From May 2009 onward, the complete ice column warmed at the CHINARE site, with a distinct lag in lower

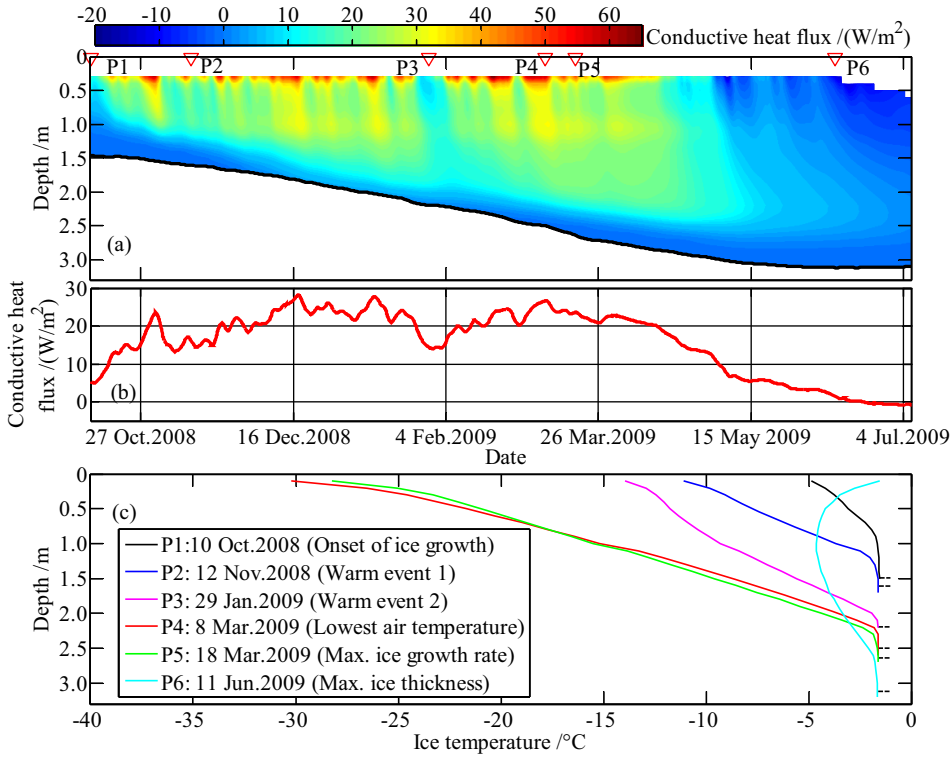

Figure 4. (a) Conductive heat fluxes through sea ice, (b) vertical average conductive heat fluxes, and (c) the typical sea-ice temperature profiles from depth 0.10 m downward at the CHINARE site. Triangles in Figure 4a denote times when the typical ice temperature profiles were observed, and black dashed lines in Figure 4c represent the ice bases.

layers because of thermal mass of the ice and the brine within the ice. With summer impending, the ice crystals surrounding brine pockets melted and enlarged the latter. The heat, afforded to melt the ice, in part counteracted the gain of thermal heat from atmosphere, hence delaying ice warming.

3.3. Conductive Heat Flux Through Ice Cover

[13] We investigated bulk conductive heat flux for layers of 0.3 m thickness, from the 0.10 m depth to the base. The measurement by the sensor at the ice surface was not used here because the ice surface was recovered by the snow after the buoy deployment. From then on, this sensor was kept in the snow cover where the thermal conductivity was relatively high.

[14] The conductive heat flux was estimated as

$$F_c = k_{si}\frac{\partial T_{si}}{\partial Z_{si}}, \qquad (1)$$

where F_c is the conductive heat flux, k_{si} is the sea ice thermal conductivity, and $(\partial T_{si}/\partial z_{si})$ is the vertical ice temperature gradient. k_{si} is a function of sea ice temperature and salinity [*Untersteiner*, 1961]. To calculate k_{si}, we used ice temperatures measured by the IMB, and assigned ice salinities 0.2, 1.5, and 8 PSU for the top 0.5 m, 0.5–1.5 m section, and section below 1.5 m, respectively. These values reflected salinities measured on the site at buoy deployment (Figure 2a) and the typical salinity for newly formed ice under multiyear sea ice [e.g., *Cox and Weeks*, 1974; *Nakawo and Sinha*, 1981].

[15] The conductive heat flux in the upper ice layer showed short-term fluctuation, in response to the diurnal changes in air temperature and the synoptic-scale atmospheric forcing (Figure 4a). The magnitudes of variations in and the absolute values of F_c diminished from top to bottom. Peaks of F_c in the deeper layer also lagged those in the upper layer. The IMB data revealed two distinct local minima of F_c in the first half of November 2008 and from late January to late February 2009. Both have been related to the passage of relatively warm and sustained synoptic systems (Figure 3b). The influence of synoptic systems on the lower ice layers was weak but longer lasting than those in the upper ice.

[16] The vertically average F_c increased markedly as atmospheric cooling from autumn to winter (Figure 4b). This flux reached its annual maximum by mid-December 2008, remaining high until late March 2009, when it started to decrease gradually due to the warming of near-surface atmosphere as well as the increased ice thickness. Later in spring and summer, the temporal lag of warming of the ice in the middle and low layers contributed to vertical inversions of ice temperature. For example, the vertical ice temperature profile on 11 June 2009 showed an obvious inversion at about 1.00 m depth (Figure 4c). Consequently, the associated transports of thermal energy into the interior of the sea ice, downward at the top and upward at the base, induced further internal ice warming and/or melt. By late

June 2009, the vertically integrated F_c changed to be negative, implying a downward flux from then on.

3.4. Heat Balance at Ice Base

[17] At the ice base the thermal fluxes combine into the heat balance:

$$F_c + F_l + F_s - F_w = 0, \tag{2}$$

where F_w represents the oceanic heat flux, F_l is the equivalent latent heat flux due to ice freezing or melt, and F_s is the specific heat flux caused by changes in ice temperature. The sign convention is such that upward, melting, and warming heat fluxes are positive, and vice versa. The latent and specific heat fluxes were calculated following *Semtner* [1976]:

$$F_l = -\rho_{si} L_f \frac{\partial z_{si}}{\partial t} \tag{3}$$

$$\text{and } F_s = \rho_{si} c_{si} \frac{\partial T_{si}}{\partial t}, \tag{4}$$

where L_f is sea ice latent heat of fusion, $(\partial z_{si}/\partial t)$ is the ice growth rate, ρ_{si} is the sea ice density, c_{si} is the sea ice specific heat, and $(\partial T_{si}/\partial t)$ is the temporal gradient in the ice temperature. The latent and specific heat of sea ice are functions of its temperature and salinity [*Untersteiner*, 1961; *Yen et al.*, 1991]. Equation (2) can then be solved for the oceanic heat flux. Due to the nonlinearity of vertical ice temperature profile, the selection of the reference level is crucial for the F_c calculation. Thus, this reference level is always chosen to avoid the basal ice layer, where the temperature gradient is low. *McPhee and Untersteiner* [1982] defined this level at 0.50 m from ice surface for ice with a thickness of 0.50–0.90 m. *Perovich et al.* [1989] defined this level at 2.00 m from ice surface for ice with a thickness of 2.75–2.98 m, while *Perovich et al.* [1997] defined this level at 1.75 m from ice surface for ice with a thickness of 2.13–2.58 m. *Lei et al.* [2010] defined this level at 0.08 m from the ice base for ice thinner than 0.50 m, and 0.12 m from the ice base for ice with a thickness of 0.50–1.73 m. In our case, a reference layer was defined at 0.40–0.70 m above the ice base, i.e., the layer demarcated by the yellow and blue dashed lines in Figure 3f. F_c is assigned as the heat flux through this layer. F_s refers to the temporal variation of ice temperature below this layer, and F_l refers to basal ice growth or decay. To calculate F_l, we assumed an ice density of 910 kg/m^3 and an ice salinity of 12 PSU. The ice growth rate was calculated as the temporal changes in ice draft as derived by the under-ice sounder. Because the sites of the under-ice sounder and the thermistor string were adjacent to each other (~2.5 m) and had near identical ice thicknesses at the deployment, the difference in ice growth rate, and consequently the F_l between two sites was ignored here. To calculate F_c and F_s, we used the mean temperature of the reference layer and that of the layer below. The ice density was set to 910 kg/m^3 and the ice salinity to 8 PSU, since both F_c and F_s related to the layers formed most recently. We chose a higher salinity for F_l than for F_c and F_s, because F_l related to the freshly formed ice layer at the bottom.

[18] Heat fluxes using a 20 day running mean are shown in Figure 5, to highlight seasonal variability. From the

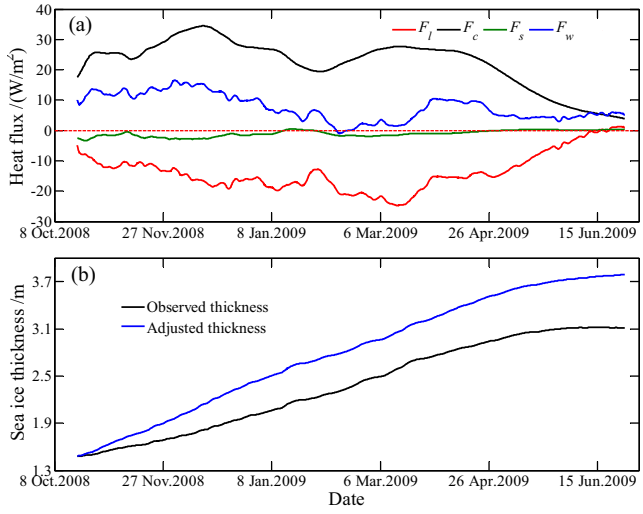

Figure 5. (a) Heat fluxes at the ice base; (b) the observed sea ice thickness, and the adjusted sea ice thickness calculated on basis of energy balance but disregarding the oceanic heat flux at the CHINARE site.

onset of basal ice growth in autumn 2008, the absolute value of F_l increased toward its annual maximum in mid-March 2009, after which it decreased. By the end of June 2009, F_l crossed the zero line and stayed positive for the remaining time. Compared with other fluxes, F_s was small throughout the investigation. Prior to May 2009, F_s was negative, indicating cooling at the ice base, except from late January to early February 2009, when ice temperature in the entire column rose sharply because of an atmospheric warm event. From May 2009 onward, the ice column warmed and F_s remained positive. From the start of the ice growth, cooling of the upper ice layers increased F_c. By mid-December 2008, the ice had thickened sufficiently to insulate itself from extensive heat loss, thereby reducing the conductive heat flux. From mid-April 2009 onward, F_c declined with persistent warming in the upper layers. F_w remained relatively high (10–15 W/m^2) during the initial ice growth until the end of December 2008. This was consistent with warm upper-ocean temperature (Figure 3e). Thus, this relatively large oceanic heat flux was attributed to the heat deposited in the upper ocean during the preceding summer and early autumn. From the beginning of January, the derived F_w decreased gradually to 0 W/m^2 by mid-February 2009, corresponding to the cooling of upper ocean. For the next 6 weeks F_w remained low, at 0–3.5 W/m^2. However, in April 2009 when the IMB drifted across the Lomonosov Ridge, there was a clear increase in F_w, to about 10 W/m^2. This was likely associated with the entrainment of deep water into the upper ocean due to bathymetric steering (shallowest depth −305 m). The water mixed upward would have had relatively high salinity, with scope to move the upper-ocean temperature above the freezing point. Oceanographic measurements have provided evidence of such salinity front over the shallow region of the Lomonosov Ridge [*Morison et al.*, 1998], where the deep water had a salinity of about 34.8 PSU. Assuming this water retained its salinity during upwelling, the departure of upper-ocean temperature above the freezing point could

be estimated at 0.2 K for the range of seawater temperature observed here. This increase in F_w slowed ice growth rate by about 0.006 m/d. Similar results pertaining to the influence of shallow bathymetry on oceanic heat flux has been obtained at the Yermak Plateau, north of Svalbard [*McPhee et al*., 2003], and Chukchi Cap [*Shaw et al*., 2009; *Perovich and Elder*, 2002]. By early May 2009, our derived F_w reverted to relatively small values ($\sim$5 W/m^2) and remained low through to the end of the IMB operation, when at which stage the IMB had drifted into the Amundsen Basin.

[19] To assess the effect of the oceanic heat flux we extremely set it to 0 W/m^2 and approximately scale the conductive heat flux inversely proportional to ice thickness as:

$$F_{ci}^{\mathrm{J}} = F_{ci}\frac{Th_{i-1}}{Th_{i-1}^{\mathrm{J}}}, \tag{5}$$

where F_{ci} and F_{ci}^{J} are the original and adjusted conductive heat flux at the time of i, and Th_{i-1} and Th_{i-1}^{J} are the original and adjusted ice thickness at the time of $i-1$ (time step for the calculation is 0.25 d). Without the oceanic forcing, the simulated ice thickness increased to 3.79 m by mid-June 2009 (Figure 5b). The simulated net increase of ice thickness is 1.4 times that observed, emphasizing the crucial role of oceanic heat flux to the basal ice mass balance.

3.5. Potential Errors in Heat-Flux Estimation

[20] Here, we present the error ranges for derived heat fluxes. For the derived F_c, potential error arises from any uncertainty in ice salinity and temperature. By setting constant ice salinities, we neglected their temporal evolution. We thus estimated the full range of variability by setting ice salinities of the top 0.5 m layer and middle layer at 0.5–1.5 m to 0 PSU. Consequently, F_c of the two upper layers increased by 0.04 W/m^2 (0.1%) and 0.28 W/m^2 (1.5%), respectively. In the newly formed ice below 1.5 m depth, ice salinity was expected to remain high during the growth season [*Cox and Weeks*, 1974; *Nakawo and Sinha*, 1981]. An assumed ice salinity from 4 to 12 PSU, which embraces the most probable values for Arctic basal ice layer during the growth season [*Nakawo and Sinha*, 1981], yields a potential error $\pm$1.2 W/m^2 ($\pm$10%) for F_c. Prior to the deployment, sensors in the thermistor string were coherent each other at $\pm$0.08 K. This corresponds to error $\pm$0.4 W/m^2 in conductive heat flux for reference layer of 0.30 m.

[21] Estimation errors of the F_c, F_s, and F_l may propagate to the F_w. Potential F_s error arises from any uncertainty in ice salinity, temperature, and density. A change in ice salinity from 4 to 12 PSU increases F_s by 0.009 W/m^2 (0.3%). For newly formed basal ice, ice density remains high in the growth season. Changing that density from 900 to 920 kg/m^3 increases F_s by 0.06 W/m^2 (2%). Thus, the potential F_s error from uncertainty in the ice density is $\pm$0.03 W/m^2 ($\pm$1%). Accuracy of the thermistor string is 0.1 K, which results in an uncertainty $\pm$0.12 W/m^2 ($\pm$4%) in specific heat flux for a 20 day average. Potential F_l error comes from any uncertainty in ice temperature, salinity, density, and growth rate. The observed range of salinity for surface seawater in the central Arctic is about 30–34 PSU [*Polyakov et al*., 2003]. Consequently, the freezing point varies from -1.62°C to -1.84°C, corresponding to an F_l increase of 1.1 W/m^2 (8.1%). The freshly formed ice layer at the bottom has significant brine entrapment [*Wettlaufer et al*., 1997; *Hunke et al*., 2011]. Changing ice salinity from 9 to 15 PSU decreases F_l by 4.6 W/m^2 (28.8%). Thus, the potential F_l error is $\pm$2.3 W/m^2 ($\pm$14.4%), owing to setting a constant ice salinity. An increase in ice density from 900 to 920 kg/m^3 raises F_l by 0.3 W/m^2 (2.2%). Thus, the potential F_l error is $\pm$0.15 W/m^2 ($\pm$1.1%), caused by setting a constant ice density. The accuracy of $\pm$0.01 m in the ice thickness measurement equates to $\pm$2.4 MJ/m^2 in equivalent latent heat. Over a 20 day interval, this amounts to a latent heat flux of 1.4 W/m^2 (8.8%).

Table 1. Potential Error in Estimation of Heat Fluxes[a]

	Heat Flux					
Error Source	F_{c1}	F_{c2}	F_{c3}	F_s	F_l	F_w
Temperature-sensor coherence	*S*	*S*	*S*	–	–	*S*
Ice temperature	–	–	–	*S*	–	*S*
Salinity of surface seawater	–	–	–	–	*M*	*M*
Ice salinity	*N*	*S*	*M*	*N*	*C*	*M*
Ice density	–	–	–	*N*	*S*	*S*
Ice growth rate	–	–	–	–	*M*	*M*

[a]Here F_{c1}, F_{c2}, and F_{c3} denote conductive heat fluxes through the ice at the depths of 0.1–0.5 m, 0.5–1.5 m, and below 1.5 m. *N*, *S*, *M*, and *C* denote negligible, minor, moderate, and crucial errors. Dashes (–) indicate inapplicable.

[22] We divided potential errors into four ranges: (a) negligible, less than 0.1 W/m^2, (b) minor, 0.1–0.5 W/m^2, (c) medium, 0.5–1.5 W/m^2, and (d) crucial, greater than 1.5 W/m^2 (Table 1). Both the coherence and precision of temperature sensors in the thermistor string are expected to influence F_c, F_s and F_w only slightly. Thus, the design of the thermistor string is appropriate. Uncertainty of the surface seawater salinity moderately affects F_l and F_w. Seawater salinity changes regionally and over time. Thus, we recommend installation of a conductivity sensor in the IMB [e.g., *Lewis et al*., 2011]. Sea ice salinity forms part of all flux estimates, and especially drives error in F_l. A nondestructive measurement technique for ice salinity has been developed by *Notz et al*. [2005]. This equipment also can be used to explore the solid fraction within the ice, thus integration of which may improve an IMB. In the F_w calculation, the error in F_l from uncertainty in ice salinity may be partly counteracted by that in F_c, because they mostly have opposing signs. Thus, the uncertainty in ice salinity is crucial for F_l, but may not be so for F_w. Ice density may slightly influence the estimates of F_l and F_w. However, since ice density in the reference layer has no known variation in the growth season, we deem the static density used here to be acceptable. The precision of ice growth rate is expected to impact F_l and F_w moderately. *Lei et al*. [2009] developed an apparatus for monitoring ice thickness based on the magnetostrictive-delay-line principle, which has a precision of $\pm$0.002 m. One might consider integrating such a device to improve the IMB.

4. Discussion

4.1. Influences on Oceanic Heat Flux and Ice Growth

[23] Most variations of F_w can be parameterized as a function of the departure of upper-ocean temperature from

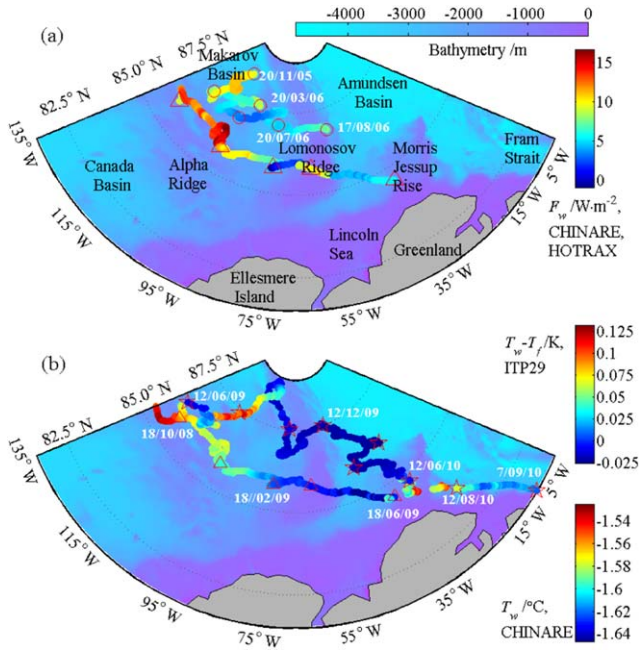

Figure 6. (a) Spatial variations in F_w at the CHINARE and HOTRAX sites; (b) seawater temperature (T_w) at depths 3.5–4.0 m at the CHINARE site and the departure of the seawater temperature (T_w) from the freezing point (T_f) at depth 12 m at the ITP29 site. Triangles, circles, and asterisks mark 2 month locations along the trajectories of the CHINARE, HOTRAX, and ITP29 buoys, respectively.

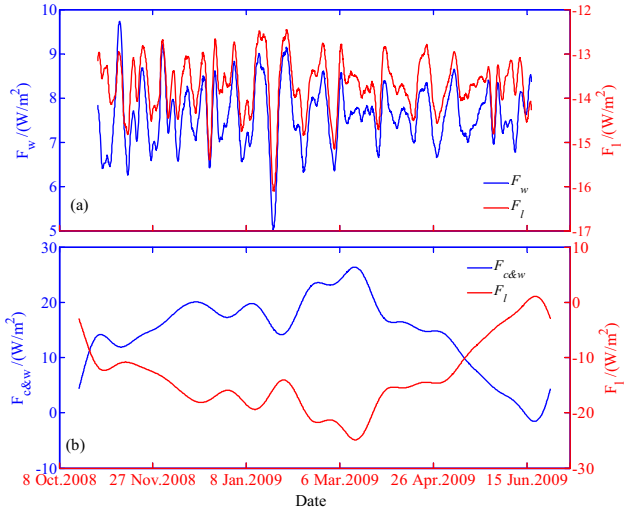

Figure 7. (a) High-frequency variations of F_l and F_w, and (b) low-frequency variations of F_l and combined component F_c and F_w at the CHINARE site.

the freezing point, and the friction speed between ice base and upper ocean [*McPhee et al.*, 2008]. In a simplistic sense, ice speed can be considered as a surrogate for turbulent mixing, because surface ocean current is mostly slow relative to the ice drift. However, in this study, significant coherence between peaks of oceanic heat flux and those of ice drift speed were not detected. This implies that change in ice speed did not exert a crucial influence on the oceanic heat flux, which in our case was regulated by the variation of heat storage in the upper ocean.

[24] Due to the lack of salinity data from the surface ocean, we cannot derive the upper-ocean freezing point. Instead, we explored the relationships between the upper-ocean temperature and the oceanic heat flux. Although the accuracy of the thermistor string (0.1 K) was not sufficient to completely observe changes in seawater temperature, we found that about 63% (square of correlation coefficient, $p < 0.01$) of oceanic heat flux could be explained by the observed upper-ocean temperature. The cooling trend in upper-ocean temperature from autumn to early spring and the warming trend in summer were coincident with seasonality of the oceanic heat flux, apart for the IMB's drift across the Lomonosov Ridge.

[25] By setting demarcations at longitudes 95°W, 70°W, and 50°W along the IMB trajectory between the Alpha Ridge, Makarov Basin, Lomonosov Ridge, and Amundsen Basin, we derived regional averages for oceanic heat fluxes 12.8, 4.8, 5.9, and 4.8 W/m^2, respectively. It appears that the oceanic heat fluxes over the ridges were greater than those over deeper water. The relatively large flux over the Alpha Ridge and small flux over the Makarov Basin may also be explained by seasonal evolution in upper-ocean temperature (Figure 6). However, the local maximum flux over the Lomonosov Ridge did not correspond to this seasonality. Therefore, this local peak was attributed mainly to upwelling of salty deep water that caused a salinity front and increase in departure of upper-ocean temperature from freezing. As shown in Figure 6, the departure of upper-ocean temperature from freezing at depth 12 m (derived from ITP29) had seasonal variations similar to those of the oceanic heat flux and upper-ocean temperature from the CHINARE IMB. However, when the ITP29 drifted across the Lomonosov Ridge, the derivation of seawater temperature from freezing did not show any rise, which implied that the oceanic heat flux under the ITP29 floe did not increase. At this stage, the ITP29 drifted about 200 km north relative to our buoy, where the shallowest depth was −1115 m. Thus, we infer that the seabed along the ITP29 track could not induce sufficient upwelling of salty deep water.

[26] Regional ice concentration can affect the oceanic heat flux by modulating the absorption of solar radiation in the upper ocean during summer [*Perovich*, 2011]. Although our data were collected when ice concentration was consistently high, the effect of summer heat deposited in the upper ocean was evident in time series of upper-ocean temperature and oceanic heat flux, with relatively high values in autumn and early winter (Figures 3e and 5).

[27] Daily mean heat fluxes at the ice base were low-pass and high-pass filtered through Fast Fourier Transform (FFT), using a threshold of 20 days. Seventy-one percent of high-frequency variations in F_l were explained by F_w ($p < 0.01$) (Figure 7a). As mentioned above, the precision of ice growth rate is expected to impact F_l and F_w moderately. Thus, the relatively high correlation between the high-frequency variations of F_l and those of F_w could be partly attributed to that the short-term changes in ice growth were mainly associated with oceanic forcing, and

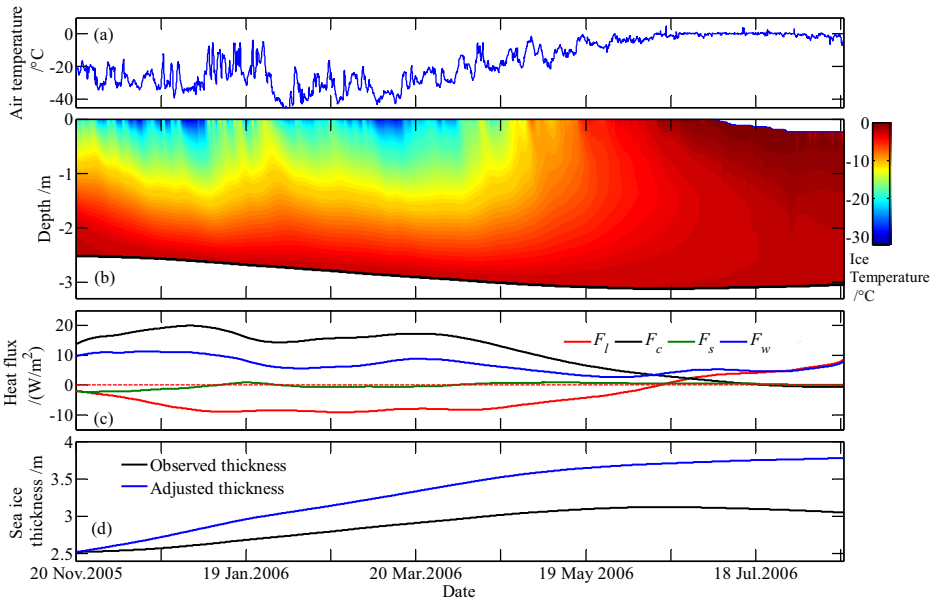

Figure 8. (a) Surface air temperature, (b) sea ice temperature, (c) heat fluxes at ice base, and (d) the observed ice thickness and the adjusted ice thickness calculated on basis of energy balance but disregarding the oceanic heat flux at the HOTRAX site.

partly attributed to that the measurement error of the under-ice sounder might propagate to both variables. In contrast, the low-frequency variations in F_l were mainly controlled by F_c and F_w, which were combined into a joint heat flux, hereafter referred to as $F_{c\&w}$ (Figure 7b). Ninety-eight percent of low-frequency variations in F_l were explained by those in $F_{c\&w}$ ($p < 0.001$). Thus, the seasonality of ice growth was jointly dominated by atmospheric and oceanic forcing.

[28] Snow accumulation over the ice can exert a crucial role on the heat flux within the ice and consequently the ice mass balance by twofold effects: (1) enhancing thermal insulation due to its relatively high thermal conductivity [*Sturm et al*., 2002] and relatively large albedo [*Perovich et al*., 2002], and (2) modulating heat balance due to the formations of slush and/or snow/superimposed ice [*Granskog et al*., 2006; *Cheng et al*., 2008]. However, uncertainties in the depth and other geophysical properties of snow hamper us to quantitatively characterizer the effect of snow cover on thermodynamic processes of ice.

4.2. Comparison with Other Studies

[29] Heat fluxes at ice base of the HOTRAX site were also estimated based on the energy balance from 10 November 2005 to 29 August 2006 when the buoy drifted across the Makarov Basin and Lomonosov Ridge. The forcing from surface atmosphere and the upper ocean was comparable for the HOTRAX and CHINARE sites from mid-November to mid-June. They had freezing degree days of 4344 and 4608 K·days, plus average oceanic heat fluxes of 7.2 and 7.1 W/m^2, respectively. The relatively thick ice thickness at the HOTRAX site resulted in later onset of ice growth (by 1.5 months) and less conductive heat flux relative to those at the CHINARE site. The difference of ice thicknesses was gradually counteracted by the difference of ice growth rates. This caused cessation of ice growth at the HOTRAX site at the same time of year (mid-June) as the CHINARE site (Figure 8b). The net increase in ice thickness at the HOTRAX site (0.61 m) was only 35% of that at the CHINARE site (1.76 m).

[30] The HOTRAX oceanic heat flux was also relatively large in autumn and early winter (Figure 8c). It decreased as winter approached, and increased again after mid-July 2006. The bathymetric effect of Lomonosov Ridge on the HOTRAX oceanic heat flux was not as strong as that on the CHINARE flux. This was attributed to a difference in the bathymetric regimes of the two trajectories. Over the Lomonosov Ridge, the shallowest ocean along the HOTRAX track was 1170 m deep, comparable to that along the ITP29 track. Mean oceanic heat fluxes under the HOTRAX site across the Makarov Basin and Lomonosov Ridge were 7.5 and 4.8 W/m^2, respectively. To assess the effect of the oceanic heat flux, we also set the HOTRAX oceanic heat flux to 0 W/m^2 and scale the conductive heat flux inversely proportional to ice thickness. The simulated HOTRAX ice thickness increased from 2.41 m in late November 2005 to 3.70 m by mid-June 2006 (Figure 8d), about twice that observed.

[31] At the SHEBA camp, *Perovich and Elder* [2002] estimated an annual average oceanic heat flux of 7.5 W/m^2, with monthly averages from 1 to 16 W/m^2. For a floe drifting northeast of Fram Strait between October and mid-November, the estimated oceanic heat flux was 0−35 W/m^2, with mean 15.3 W/m^2 [*Wettlaufer*, 1991]. For a floe drifting in the Beaufort Sea from May to November, the estimated oceanic heat flux was 5–9 W/m^2 [*Perovich et al*., 1997]. Thus, the oceanic heat flux derived here falls within the range of previous studies.

5. Conclusions

[32] Data obtained from an IMB operating in the central Arctic from August 2008 to July 2009 were used to explore

the thermal regimes of an ice floe along its Lagrangian trajectory. The ice melted from 1.95 m in late August 2008 to 1.46 m by mid-October 2008. The ice growth season went from then on, and terminated by mid-June 2009. During this time, ice thickness increased to 3.12 m. From comparisons with the HOTRAX IMB, operating in 2005/2006 slightly to the north, the conductive heat flux through the ice column and the ice growth rate were strongly dependent on ice thickness.

[33] Both ice temperature and conductive heat flux in the top layer had persistent high-frequency variations, which were attenuated and time-lagged in deeper layers. It seems that diurnal or synoptic-scale atmospheric processes do not generally produce marked changes in ice mass balance at ice base. The ice cover serves as a thermal "flywheel" due to its thermal inertia, maintaining a relatively steady ice growth despite large swings in atmospheric forcing. At the beginning of ice growth season, oceanic heat flux was relatively large at 10–15 W/m^2, which could be attributed to the heat storage in the upper ocean during summer and early autumn. Oceanic heat flux decreased gradually from December 2008, approaching 0 W/m^2 by mid-February 2009. Afterward, the heat flux remained weak through to the end of IMB operation, with the exception of April 2009 when it increased as the buoy crossed the Lomonosov Ridge. This increase was due to upward turbulent mixing of salty deep water. However, from the data of ITP29 and the HOTRAX IMB, the effect of bathymetry on the oceanic heat flux was not evident in the region 1–2° north from the CHINARE track across the Lomonosov Ridge. There, the submarine ridge does not rise as high as beneath the CHINARE buoy track. Without any oceanic heat flux, the annual net basal ice growth may have increased by 40% and 100% at the CHINARE and HOTRAX sites, respectively. Thus, the influence of the oceanic heat flux on ice mass balance is more crucial for thick ice than thin ice, because of the relatively small conductive heat flux through thick ice. Due to thinning of Arctic sea ice, the role of conductive heat flux on ice mass balance may be enhanced.

[34] Uncertainties in the salinities of surface seawater and sea ice, as well as in basal ice growth rate, were the dominant error sources in the estimation of basal latent heat flux. Uncertainty in sea ice salinity also dominated the error in deriving the basal conductive heat flux. Reducing these uncertainties is the primary consideration to optimize the estimation of the oceanic heat flux via the energy balance method.

[35] **Acknowledgments.** This work was supported by grants from the National Natural Science Foundation of China (41106160 and 40930848) and Chinese Polar Environment Comprehensive Investigation and Assessment Programs (CHINARE2013-04-03 and CHINARE2013-04-04). PH's contributions to this project were supported by the Australian Governmental Cooperative Research Centre Program through the Antarctic Climate and Ecosystems Cooperative Research Centre, and by AAD through AAS grants 3328 and 4072. We thank S. E. Lake for grammatical checks. We also thank the anonymous reviewers for their comments, which enabled us to greatly improve this publication.

References

Cheng, B., Z. Zhang, T. Vihma, M. Johansson, L. Bian, Z. Li, and H. Wu (2008), Model experiments on snow and ice thermodynamics in the Arctic Ocean with CHINARE 2003 data, *J. Geophys. Res.*, *113*, C09020, doi:10.1029/2007JC004654.

Cox, G. F. N., and W. F. Weeks (1974), Salinity variations in sea ice, *J. Glaciol.*, *13*(67), 109–120.

Hunke, E. C., D. Notz, A. K. Turner, and M. Vancoppenolle (2011), The multiphase physics of sea ice: A review for model developers, *Cryosphere*, *5*, 989–1009, doi:10.5194/tc-5-989-2011.

Granskog, M. A., T. Vihma, R. Pirazzini, and B. Cheng (2006), Superimposed ice formation and surface fluxes on sea ice during the spring melt-freeze period in the Baltic Sea, *J. Glaciol.*, *52*(176), 119–127, doi:10.3189/172756506781828971.

Jakobsson, M., R. Macnab, L. Mayer, R. Anderson, M. Edwards, J. Hatzky, H. W. Schenke, and P. Johnson (2008), An improved bathymetric portrayal of the Arctic Ocean: Implications for ocean modeling and geological, geophysical and oceanographic analyses, *Geophys. Res. Lett.*, *35*, L07602, doi:10.1029/2008GL033520.

Kistler, R., et al. (2001), The NCEP-NCAR 50-year reanalysis: Monthly means CD-ROM and documentation, *Bull. Am. Meteorol. Soc.*, *82*, 247–268.

Laxon, S. W., et al. (2013), CryoSat-2 estimates of Arctic sea ice thickness and volume, *Geophys. Res. Lett.*, *40*, 732–737, doi:10.1002/grl.50193.

Lei, R., Z. Li, Y. Cheng, X.Wang, and Y. Chen (2009), A new apparatus for monitoring sea ice thickness based on the magnetostrictive-delay-line principle, *J. Atmos. Oceanic Technol.*, *26*(4), 818–827, doi:10.1175/2008JTECHO613.1.

Lei, R., Z. Li, B. Cheng, Z. Zhang, and P. Heil (2010), Annual cycle of landfast sea ice in Prydz Bay, east Antarctica, *J. Geophys. Res.*, *115*, C02006, doi:10.1029/2008JC005223.

Lei, R., Z. Li, N. Li, P. Lu, and B. Cheng (2012), Crucial physical characteristics of sea ice in the Arctic section of 143°W–180°W during August and early September 2008, *Acta Oceanol. Sin.*, *31*(4), 65–75.

Leppäranta, M., and T. Manninen (1988), The brine and gas content of sea ice with attention to low salinities and high temperatures, Rep. 88–2, Finnish Inst. for Mar. Res., Helsinki.

Lewis, M. J., J. L. Tison, B. Weissling, B. Delille, S. F. Ackley, F. Brabant, and H. Xie (2011), Sea ice and snow cover characteristics during the winter–spring transition in the Bellingshausen Sea: An overview of SIMBA 2007, *Deep Sea Res. Part II*, *58*, 1019–1038.

McPhee, M. G. (1992), Turbulent heat flux in the upper ocean under sea ice, *J. Geophys. Res.*, *97*(C4), 5365–5379, doi:10.1029/92JC00239.

McPhee, M. G., and N. Untersteiner (1982), Using sea ice to measure vertical heat flux in the ocean, *J. Geophys. Res.*, *87*, 2071–2074.

McPhee, M. G., T. Kikuchi, J. H. Morison, and T. P. Stanton (2003), Ocean-to-ice heat flux at the North Pole environmental observatory, *Geophys. Res. Lett.*, *30*(24), 2274, doi:10.1029/2003GL018580.

McPhee, M. G., J. H. Morison, and F. Nilsen (2008), Revisiting heat and salt exchange at the ice-ocean interface: Ocean flux and modeling considerations, *J. Geophys. Res.*, *113*, C06014, doi:10.1029/2007JC004383.

Morison, J., M. Steele, and R. Andersen (1998), Hydrography of the upper Arctic Ocean measured from the nuclear submarine U.S.S. Pargo, *Deep Sea Res.* Part I, *45*, 15–38.

Nakawo, M., and N. K. Sinha (1981), Growth rate and salinity profile of first-year sea ice in the high Arctic, *J. Glaciol.*, *27*(96), 315–330.

Notz, D., J. S. Wettlaufer, and M. G. Worster (2005), A non-destructive method for measuring the salinity and solid fraction of growing sea ice in situ, *J. Glaciol.*, *51*, 159–166, doi:10.3189/172756505781829548.

Perovich, D. K. (2011), The changing Arctic sea ice cover, *Oceanography*, *24*(3), 162–173.

Perovich, D. K., and B. C. Elder (2002), Estimates of ocean heat flux at SHEBA, *Geophys. Res. Lett.*, *29*(9), 1344, doi:10.1029/2001GL014171.

Perovich, D. K., W. B. Tucker III, and R. A. Krishfield (1989), Oceanic heat flux in the Fram Strait measured by a drifting buoy, *Geophys. Res. Lett.*, *16*, 995–998, doi:10.1029/GL016i009p00995.

Perovich, D. K., B. C. Elder, and J. A. Richter-Menge (1997), Observations of the annual cycle of sea ice temperature and mass balance, *Geophys. Res. Lett.*, *5*, 555–558.

Perovich, D. K., T. C. Grenfell, B. Light, and P. V. Hobbs (2002), Seasonal evolution of the albedo of multiyear Arctic sea ice, *J. Geophys. Res.*, *107*(C10), 8044, doi:10.1029/2000JC000438.

Perovich, D. K., T. C. Grenfell, B. Light, B. C. Elder, J. Harbeck, C. Polashenski, W. B. Tucker III, and C. Stelmach (2009), Transpolar observations of the morphological properties of Arctic sea ice, *J. Geophys. Res.*, *114*, C00A04, doi:10.1029/2008JC004892.

Perovich, D. K., J. A. Richter-Menge, K. F. Jones, B. Light, B. C. Elder, C. Polashenski, D. Laroche, T. Markus, and R. Lindsay (2011), Arctic sea-ice melt in 2008 and the role of solar heating, *Ann. Glaciol.*, *52*(57), 355–359.

Polyakov, I., D. Walsh, I. Dmitrenko, R. L. Colony, and L. A. Timokhov (2003), Arctic Ocean variability derived from historical observations, *Geophys. Res. Lett.*, *30*, 1298, doi:10.1029/2002GL016441.

Rampal, P., J. Weiss, and D. Marsan (2009), Positive trend in the mean speed and deformation rate of Arctic sea ice, *1979–2007*, J. Geophys. Res., 114, C05013, doi:10.1029/2008JC005066.

Richter-Menge, J. A., D. K. Perovich, B. C. Elder, K. Claffey, I. Rigor, and M. Ortmeyer (2006), Ice mass balance buoys: A tool for measuring and attributing changes in the thickness of the Arctic sea-ice cover, *Ann. Glaciol.*, *44*, 205–210.

Semtner, A. J. (1976), A model for the thermodynamic growth of sea ice in numerical investigations climate, *J. Phys. Oceanogr.*, *6*, 379–389.

Shaw, W. J., T. P. Stanton, M. G. McPhee, J. H. Morison, and D. G. Martinson (2009), Role of the upper ocean in the energy budget of Arctic sea ice during SHEBA, *J. Geophys. Res.*, *114*, C06012, doi:10.1029/2008JC004991.

Spreen, G., L. Kaleschke, and G. Heygster (2008), Sea ice remote sensing using AMSR-E 89 GHz channels, *J. Geophys. Res.*, *113*, C02S03, doi:10.1029/2005JC003384.

Stroeve, J. C., V. Kattsov, A. Barrett, M. C. Serreze, T. Pavlova, M. Holland, and W. N. Meier (2012), Trends in Arctic sea ice extent from CMIP5, CMIP3 and observations, *Geophys. Res. Lett.*, 39, L16502, doi:10.1029/2012GL052676.

Sturm, M., D. K. Perovich, and J. Holmgren (2002), Thermal conductivity and heat transfer through the snow on the ice of the Beaufort Sea, *J. Geophys. Res.*, *107*(C10), 8043, doi:10.1029/2000JC000409.

Timmermans, M.-L., A. Proshutinsky, R. A. Krishfield, D. K. Perovich, J. A. Richter-Menge, T. P. Stanton, and J. M. Toole (2011), Surface freshening in the Arctic Ocean's Eurasian Basin: An apparent consequence of recent change in the wind-driven circulation, *J. Geophys. Res.*, *116*, C00D03, doi:10.1029/2011JC006975.

Toole, J. M., R. A. Krishfield, M.-L. Timmermans, and A. Proshutinsky (2011), The ice-tethered profiler: Argo of the Arctic, *Oceanography*, *24*(3), 126–135.

Untersteiner, N. (1961), On the mass and heat budget of Arctic sea ice, *Arch. Meteorol. Geophys. Bioklimatol. Ser. A*, *12*, 151–182, doi:10.1007/BF02247491.

Wettlaufer, J. S. (1991), Heat flux at the ice-ocean interface, *J. Geophys. Res.*, *96*(C4), 7215–7236, doi:10.1029/90JC00081.

Wettlaufer, J. S., M. G. Worster, and H. E. Huppert (1997), The phase evolution of young sea ice, *Geophys. Res. Lett.*, *24*(10), 1251–1254.

Yen, Y. C., K. C. Cheng, and S. Fukusako (1991), Review of intrinsic thermophysical properties of snow, ice, sea ice, and frost, in *Proceedings of the 3rd International Symposium on Cold Regions Heat Transfer*, Fairbanks, AK, June 11–14, 1991, edited by J. P. Zarling and S. L. Faussett, pp. 187–218, Univ. of Alaska, Fairbanks.